Chinese Journal of
POLYMER SCIENCE

RESEARCH ARTICLE

https://doi.org/10.1007/s10118-026-3838-8
Chinese J. Polym. Sci.

Solid-additive-regulated Non-equilibrium Film Formation Enables Highly-efficient Green-solvent-printed Binary Organic Solar Cells and Solar Modules

Shan-Hua Zhang[a], Rui Sun[a,c*], Zi-Cheng Xing[a], Jia-Wang Qiu[a], Lin-Yong Xu[a], Yu-Hao Liu[a], Tian-Rui Qu[a], Xin-Rong Yang[a], and Jie Min[a,b*]

[a] *The Institute for Advanced Studies, School of Electrical Engineering and Automation, Wuhan University, Wuhan 430072, China*
[b] *Key Laboratory for Preparation and Application of Ordered Structural Materials of Guangdong Province, Shantou University, Shantou 515063, China*
[c] *Anhui Province Key Laboratory for Control and Application of Optoelectronic Information Materials, Anhui Normal University, Wuhu 241002, China*

Electronic Supplementary Information

Abstract The commercialization of organic solar cells (OSCs) requires a transition from laboratory-scale spin-coating to high-throughput, environmentally friendly printing technologies. However, rapid crystallization and non-equilibrium molecular assembly during green-solvent processing often induce disordered morphologies and severe efficiency losses. Here, we introduce two nonhalogenated solid additives, 2-methoxynaphthalene (2-MN) and 2,7-dimethoxynaphthalene (2,7-MN), to regulate crystallization kinetics and film formation in blade-coated OSCs processed from the green solvent *o*-xylene. Benefiting from its symmetric molecular structure and stronger intermolecular interactions, 2,7-MN effectively prolongs the liquid-solid transition and suppresses premature aggregation, enabling the formation of a highly ordered bi-continuous interpenetrating network with optimized charge-transport pathways. As a result, green-solvent-processed OSCs achieve a champion power conversion efficiency of 20.19% with an exceptional fill factor of 81.52%. Notably, the morphology control enabled by 2,7-MN remains robust under high-speed coating (30 m·min^{-1}), maintaining efficiencies approaching 19%. Importantly, large-area modules (15.84 and 76.95 cm^2) deliver impressive efficiencies of 16.80% and 15.71%, respectively, which are the highest values reported in green-solvent-processed OSCs so far. This work establishes solid-additive engineering as an effective strategy for controlling non-equilibrium film formation toward scalable and sustainable organic photovoltaics.

Keywords Organic solar cells; Environmentally friendly solvents; Solid additives; High-speed blade-coating; Large-area modules

Citation: Zhang, S. H.; Sun, R.; Xing, Z. C.; Qiu, J. W.; Xu, L. Y.; Liu, Y. H.; Qu, T. R.; Yang, X. R.; Min, J. Solid-additive-regulated non-equilibrium film formation enables highly-efficient green-solvent-printed binary organic solar cells and solar modules. *Chinese J. Polym. Sci.* https://doi.org/10.1007/s10118-026-3838-8

INTRODUCTION

Organic solar cells (OSCs) have emerged as promising next-generation photovoltaic technologies owing to their intrinsic advantages, including lightweight, mechanical flexibility, semi-transparency, and compatibility with low-temperature processing.[1–6] Over the past decade, OSCs have experienced remarkable progress driven by synergistic advances in molecular design, device physics, device engineering, and processing strategies. In particular, the emergence of non-fullerene acceptors (NFAs) has revolutionized the field by enabling precise energy level alignment, strong and tunable absorption, and favorable nanoscale morphology. As a result, the power conversion efficiencies (PCEs) of single-junction OSCs have recently approached 21% in laboratory-scale devices.[7–9] Such rapid efficiency improvements highlight the immense potential of OSCs for practical deployment. Despite these advances, a critical gap remains between high-efficiency laboratory devices and scalable manufacturing. Most state-of-the-art OSCs with record PCEs are fabricated *via* spin-coating, a technique that is unsuitable for large-area, high-throughput production.[10–12] More importantly, these devices typically rely on halogenated solvents, such as chloroform or chlorobenzene, to dissolve high-performance donor (D) and acceptor (A) materials and to achieve optimal film morphology. While effective at the laboratory scale, these solvents pose significant environmental, health, and safety concerns due to their toxicity, volatility, and regulatory restrictions.[4] Their use also complicates industrial implementation, as large-scale manufacturing requires stringent solvent-recovery systems and raises production costs. Consequently, transitioning from halogenated to environmentally benign, non-

* Corresponding authors, E-mail: sun.rui@whu.edu.cn (R.S.)
E-mail: min.jie@whu.edu.cn (J.M.)
Received June 16, 2026; Accepted August 10, 2026; Published online November 2, 2026

© Chinese Chemical Society
Institute of Chemistry, Chinese Academy of Sciences

halogenated ("green") solvents is widely recognized as a prerequisite for the sustainable commercialization of OSC technologies.[13]

However, the adoption of green solvents introduces substantial scientific and technological challenges. High-performance polymer donors and NFAs are typically engineered with complex conjugated backbones and bulky side chains to optimize optoelectronic properties. Still, these structural features often result in limited solubility in non-halogenated solvents such as *o*-xylene (*o*-XY), toluene, or anisole.[14,15] Poor solubility can induce strong pre-aggregation in solution, which persists during film formation and leads to kinetically trapped, non-ideal morphologies. In addition, the drying dynamics of green solvents differ significantly from those of halogenated solvents, further complicating the control of crystallization and phase separation during printing processes such as blade coating, slot-die coating, or inkjet printing.[16] These factors often result in disordered molecular packing, excessive or insufficient phase separation, and suboptimal percolation pathways for charge transport. Consequently, OSCs processed from green solvents typically exhibit inferior exciton dissociation efficiency, imbalanced charge transport, and increased recombination losses, leading to a pronounced efficiency gap compared to their halogenated-solvent-processed counterparts.[17]

To address these limitations, extensive efforts have been devoted to improving the performance of green-solvent-processed OSCs. One major approach involves molecular design, including the development of D/A materials with enhanced solubility and reduced aggregation tendencies in non-halogenated solvents.[18,19] In parallel, solvent engineering has been widely explored, including the use of binary or ternary solvent systems, high-boiling-point additives, and solvent mixtures with tailored evaporation rates to modulate film formation kinetics.[20,21] Advanced processing techniques, such as temperature-controlled coating,[21,22] solvent vapor annealing,[23] and ultrasonic-assisted deposition,[14] have also been employed to improve morphology control and device performance. Among these strategies, additive engineering has emerged as a particularly versatile and effective approach for regulating intermolecular interactions and guiding the evolution of morphology in OSC active layers.[24–27] In particular, solid additives represent an emerging class of morphology regulators that offer distinct advantages for green-solvent processing. Unlike liquid additives, which generally suffer from several drawbacks (like residual contamination and limited compatibility), solid additives can transiently interact with D/A components, modulating nucleation and growth processes, suppressing premature aggregation during film formation.[24,28] Nevertheless, the design principles governing their effectiveness, especially in the context of green-solvent printing processes, remain insufficiently understood. Key questions include how molecular symmetry, interaction strength, and volatility influence the evolution of morphology, and how these factors can be optimized to achieve both high efficiency and process robustness.

Herein, we address these challenges by introducing two environmentally benign solid additives, 2-methoxynaphthalene (2-MN) and 2,7-dimethoxynaphthalene (2,7-MN), into a D18:L8-BO binary system processed from the green solvent *o*-XY. By systematically investigating their molecular structures and interaction characteristics, we reveal the critical role of additive symmetry and intermolecular interactions in modulating crystallization kinetics and film formation. In particular, 2,7-MN, featuring a symmetric substitution pattern and stronger intermolecular interactions, effectively prolongs the liquid-solid transition stage during blade coating. This extended transition suppresses premature aggregation and enables the formation of a highly ordered bicontinuous interpenetrating network with optimized domain size and purity. The resulting morphology significantly enhances exciton dissociation, facilitates balanced charge transport, and suppresses bimolecular recombination. As a result, OSC devices processed from *o*-XY using 2,7-MN achieve PCEs exceeding 20% under blade-coating conditions, with devices fabricated at coating speeds up to 30 m·min^{-1} maintaining PCEs close to 19%. Furthermore, large-area modules with active areas of 15.84 and 76.95 cm^2 deliver PCEs of 16.80% and 15.71%, respectively, demonstrating the outstanding solution processability and module scalability.

EXPERIMENTAL

Detailed experimental procedures, including reagent sources, characterization instruments, and test conditions, are provided in the electronic supplementary information (ESI).

RESULTS AND DISCUSSION

To elucidate the underlying mechanisms by which solid additives enhance photovoltaic performance, density functional theory (DFT) calculations at the B3LYP/6-31G(d) level were performed to analyze the intermolecular interactions between 2-MN/2,7-MN and the active-layer components. Electrostatic potential (ESP) mapping reveals that the asymmetric monomethoxy-substituted 2-MN exhibits a polarized and uneven charge distribution (Fig. 1a), whereas 2,7-MN, featuring symmetric dimethoxy substitution, displays a more uniform potential distribution with pronounced positive regions.[29] Given their relatively positive surface ESP, both additives are expected to interact electrostatically with the negatively charged regions of the acceptor L8-BO, particularly near the pyrrole rings. Conversely, the ESP distribution of the donor D18 segment appears relatively homogeneous, rendering specific interaction sites less discernible from potential mapping alone (Fig. S1 in ESI). Therefore, intermolecular binding energy (E_b) was further calculated based on optimized geometries to quantify interaction strengths (Fig. 1b).[30] The results show that 2,7-MN delivers a significantly higher E_b (0.197 eV) than 2-MN (0.082 eV), indicating stronger intermolecular affinity, which may effectively suppress disordered head-to-head stacking among acceptor molecules.[31] For D18, 2-MN preferentially interacts with the electron-deficient thiadiazole segment (E_b=0.181 eV), whereas 2,7-MN tends to associate with the alkylthiophene side-chain of the benzodithiophene (BDT) unit (E_b=0.154 eV). Considering that lamellar packing in conjugated polymers is predominantly governed by side-chain arrangement, such selective interactions by 2,7-MN are expected to impose a moderate steric effect, thereby optimizing crystallization pathways. Overall, the anchoring and induc-

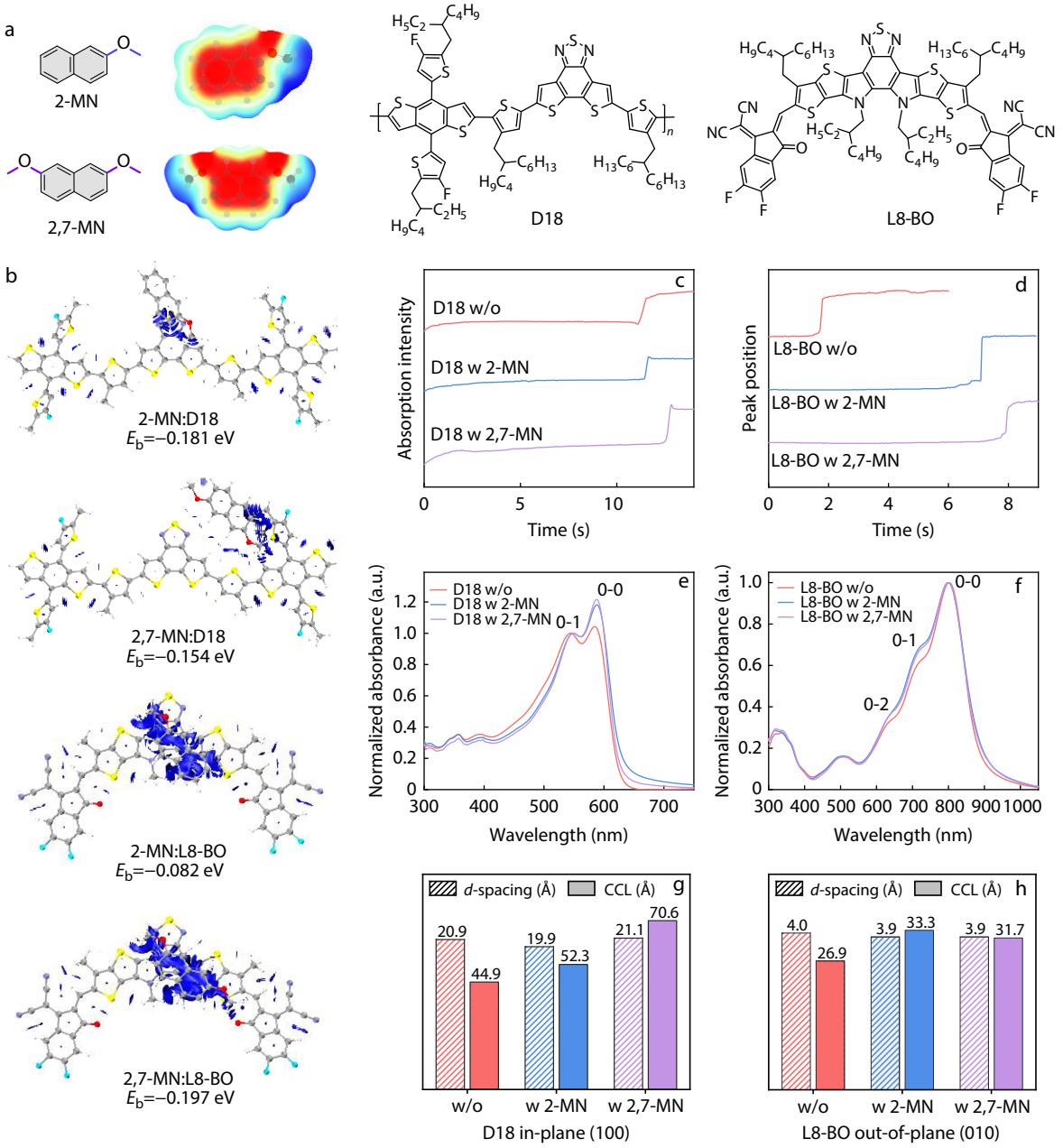


Fig. 1 (a) Molecular structures and ESP maps of the additives (potential range: –0.5 to 0.5 eV); (b) Calculated intermolecular binding energies and corresponding interaction sites between the additives and D18, L8-BO; (c, d) Film-forming kinetics curves derived from *in situ* absorption spectroscopy; (e, f) Normalized UV-Vis-NIR absorption spectra of D18 and L8-BO neat film; (g, h) Statistical plots of lamellar spacing and CCL for the D18 in-plane (100) peak, and *π*-*π* spacing and CCL for the L8-BO out-of-plane (010) peak. D18 w/o refers to the pure film of D18 that has not undergone any additive treatment. D18 w 2-MN refers to the pure film of D18 that has been treated with the 2-MN additive. D18 w 2,7-MN refers to the pure film of D18 that has been treated with the 2,7-MN additive.

tion effects introduced by 2,7-MN are expected to synergistically regulate crystallization behavior, offering a theoretical basis for morphological optimization.

To further investigate film formation dynamics, *in situ* ultraviolet-visible-near infrared (UV-Vis-NIR) absorption spectroscopy was employed to monitor the film evolution of D18 and L8-BO during blade coating (Figs. S2 and S3 in ESI). Compared with additive-free systems, both 2-MN and 2,7-MN significantly prolong the solvent evaporation stage, thereby extending the time window for molecular pre-organization in the solution state. Notably, during the liquid-solid phase transition, the 2,7-MN-treated system exhibits a notably extended transition duration, indicative of pronounced kinetic retardation. This observation is consistent with the stronger intermolecular interactions predicted by DFT calculations, suggesting that 2,7-MN acts as an effective kinetic controller that delays premature aggregation and self-assembly of D/A components (Figs. 1c and 1d).[32] Such controlled kinetics facili-

tate the formation of optimized nanoscale active layer morphology during film deposition. The impact of additives on post-deposition molecular aggregation was initially corroborated *via* UV-Vis-NIR absorption spectra (Figs. 1e and 1f). Compared to the pristine D18 film, both 2-MN and 2,7-MN treatments induce a redshift of the absorption edge and an enhancement in the $A_{0\text{-}0}/A_{0\text{-}1}$ vibronic ratio, indicative of enhanced molecular ordering. This effect is most pronounced for the 2,7-MN-processed film, suggesting that its preferential interaction with side chains more effectively promotes *J*-aggregate formation compared to the interaction of 2-MN with electron-deficient backbone units of D18.[33] For L8-BO, both additives enhance the $A_{0\text{-}1}$ and $A_{0\text{-}2}$ shoulder features and induce a slight redshift, implying suppression of rapid, disordered crystallization and a transition toward *H-J* hybrid packing aggregation.[34] Collectively, these spectral changes demonstrate that both additives facilitate the transformation of disordered phases into well-organized crystalline structures.[14]

Two-dimensional grazing-incidence wide-angle X-ray scattering (2D GIWAXS) measurements were performed to further analyze the impact of additives on the packing behaviors of D18 and L8-BO films (Figs. S4, S5 and Tables S1, S2 in ESI). In the out-of-plane (OOP) direction of D18 films, all three samples exhibit comparable OOP crystallinity, whereas significant differences are observed in the in-plane (IP, 100) lamellar packing. Specifically, 2-MN treatment results in a reduced (100) *d*-spacing of 19.9 Å (Figs. 1g and 1h), compared to 20.9 Å for 2,7-MN and 21.1 Å for the control (w/o), respectively. Crucially, the crystalline coherence length (CCL) is substantially enhanced in the 2,7-MN-treated film (70.6 Å), exceeding that of the control (44.9 Å) and 2-MN-treated films (52.3 Å). These results indicate that 2,7-MN effectively modulates side-chain packing, mitigating excessive lamellar aggregation while promoting higher aggregation order. For L8-BO, all films exhibit a predominant face-on orientation. However, the OOP (010) diffraction peaks reveal that additive-treated films possess more compact and ordered π-π stacking, with reduced *d*-spacing (3.9 Å) and increased CCLs (33.3 Å for 2-MN and 31.7 Å for 2,7-MN, respectively), compared to the control film (4.0 and 26.9 Å). These findings are consistent with absorption spectroscopy results, confirming enhanced molecular ordering induced by the additives. Overall, the improved crystallinity of both D18 and L8-BO phases, particularly in the presence of 2,7-MN, is conducive to the formation of an ordered bi-fibrillar interpenetrating network within the blend films. Moreover, the UV-Vis-NIR absorption spectra of the blend active layers exhibit slight redshifts upon additive incorporation (Fig. S6 in ESI), further corroborating the enhancement in intermolecular packing order. Collectively, these results demonstrate that solid-additive engineering, especially with structurally symmetric 2,7-MN, enables precise regulation of crystallization kinetics and molecular organization, ultimately leading to optimized morphology and improved device performance as discussed below.

To investigate the effect of solid additives on device performance, OSCs were fabricated with a conventional structure of ITO/2PACz/active layer/PNIDT-F3N/Ag. The optimal current density-voltage (*J-V*) characteristics of D18:L8-BO devices processed without and with solid additives are illustrated in Fig. 2(a) and Fig. S7 (in ESI), with the corresponding photovoltaic parameters summarized in Table 1 and Table S3 (in ESI). The control D18:L8-BO device without additive treatment delivers a PCE of 18.14%, with an open-circuit voltage (V_{OC}) of 0.900 V, a short-circuit current density (J_{SC}) of 26.48 mA·cm^{-2}, and a fill factor (FF) of 76.10%. Upon incorporation of 2-MN, a marginal improvement is observed, yielding a PCE of 18.76% with slightly enlarged J_{SC} and FF values. Notably, devices treated with 2,7-MN exhibit a pronounced performance enhancement, achieving a champion PCE of 20.19%, accompanied by an impressive FF of 81.52% and an enhanced J_{SC} of 27.28 mA·cm^{-2}. External quantum efficiency (EQE) curves (Fig. 2b) further corroborate these results, with integrated current densities ($J_{SC\ cal}$) of 25.83 and 26.40 mA·cm^{-2} for the 2-MN- and 2,7-MN-treated devices, respectively, compared to 25.79 mA·cm^{-2} for the control. To the best of our knowledge (Fig. 2c and summarized in Table S4 in ESI), this PCE (20.19%) represents one of the highest reported values for green-solvent-processed, blade-coated OSCs so far. To gain insight into the charge generation dynamics, transient absorption (TA) spectroscopy was employed. Selective excitation of the acceptor was achieved using an excitation wavelength of 800 nm. The two-dimensional TA spectra (Fig. 2d) reveal ground-state bleaching (GSB) features of D18 and L8-BO in the spectral ranges of 500–600 and 650–880 nm, respectively. The decay dynamics probed at different wavelengths represent the different photophysical processes (Fig. 2e). The emergence of the D18 GSB signal at 580 nm concomitant with the decay of the L8-BO signal at 700 nm indicates efficient hole transfer from the acceptor to the donor. Kinetic analysis of the GSB decay at 580 nm reveals a biexponential behavior, with fast (τ_1) and slow (τ_2) components. The 2,7-MN-treated blend exhibits significantly shorter τ_1 (0.67 ps) and τ_2 (14.27 ps) compared to the control (2.80 and 36.62 ps) and 2-MN-treated films (2.01 and 31.36 ps), indicating more rapid excition dissociation and diffusion toward D-A interfaces. These accelerated dynamics are consistent with the enhanced J_{SC} and FF values observed in the corresponding devices.[9,35]

Charge transport properties were further evaluated using the space charge-limited current (SCLC) method (Figs. S8, S9 and Table S5 in ESI). As summarized in Fig. 2(f), the hole mobility (μ_h) and electron mobility (μ_e) were estimated to be 7.55×10^{-4} and 1.36×10^{-4} cm^2·V^{-1}·s^{-1} for the control device. Incorporation of solid additives leads to an overall enhancement in charge carrier mobilities, attributed to enhanced molecular ordering and stacking. In particular, the 2,7-MN-treated device shows balanced charge transport with $\mu_h=3.50\times10^{-4}$ and $\mu_e=2.24\times10^{-4}$ cm^2·V^{-1}·s^{-1}, yielding a μ_h/μ_e ratio of 1.56,[36] which is favorable for efficient charge extraction and reduced recombination. Apart from the SCLC data, fifteen photo-induced charge carrier extraction by linearly increasing voltage (photo-CELIV) curves over the nanosecond-microsecond (ns-ms, Fig. S10 in ESI) have been measured using different experimental conditions for determining the ambipolar charge extraction (CE) properties from the devices with and without solid additives treatment. As exhibited in Fig. 2(g), the extracted carrier mobilities are consistent with the SCLC results. By fitting the decay using the relation

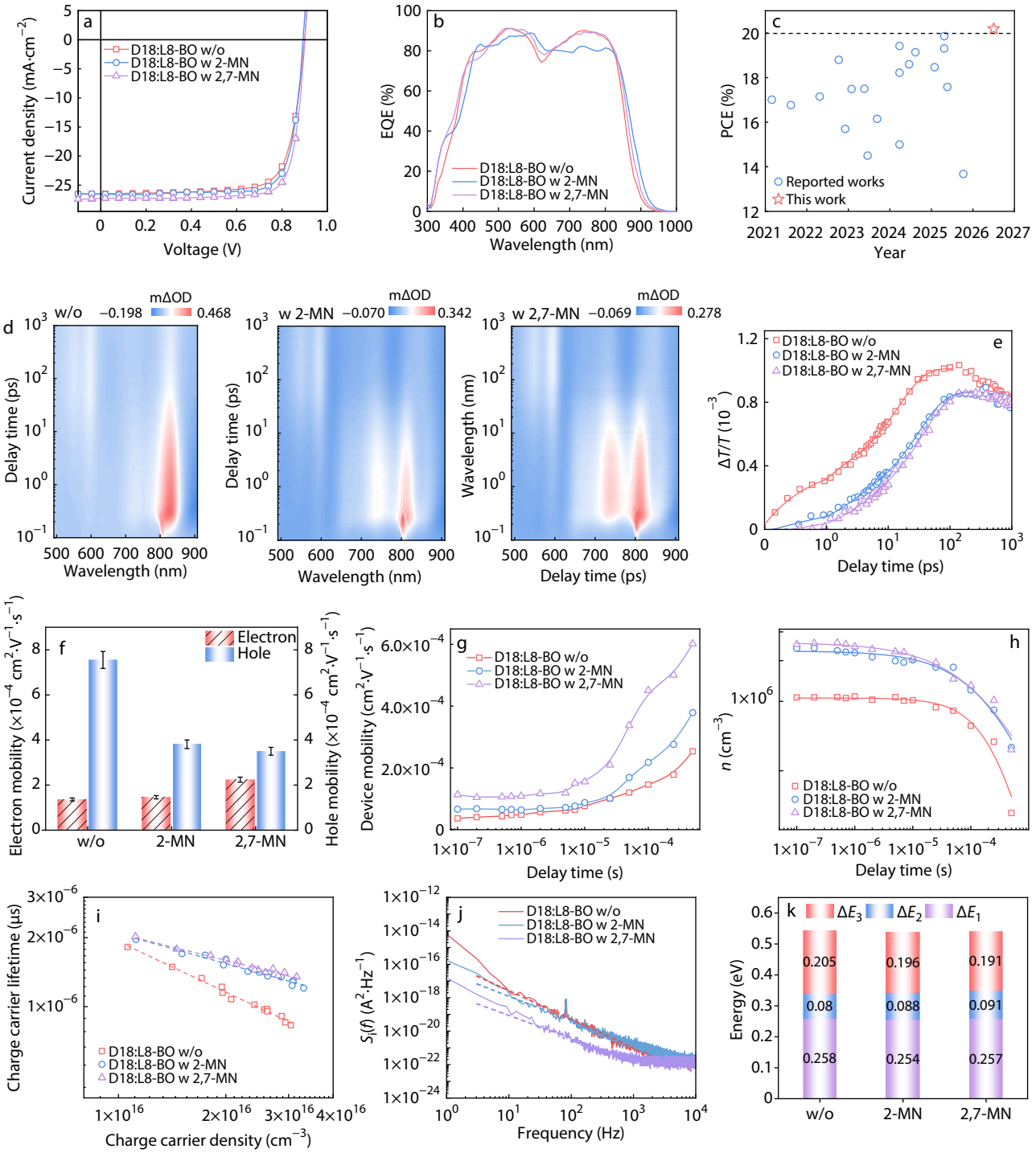


Fig. 2 (a) *J-V* curves and (b) EQE spectra of D18:L8-BO devices with and without solid additives treatment; (c) Literature-reported PCEs for state-of-the-art green-solvent-processed blade-coated OSCs; (d) 2D TA spectra and (e) decay dynamics were probed at 575 nm of the D18:L8-BO films with and without solid additives treatment under 800 nm excitation; (f) The electron and hole mobilities obtained from SCLC measurements, and (g) device mobility as a function of delay time obtained from photo-CELIV measurement of D18:L8-BO devices with and without solid additives treatment; (h) Charge carrier density as a function of delay time of the D18:L8-BO devices with and without solid additives treatment; (i) Charge carrier lifetime versus charge density curves of D18:L8-BO devices with and without solid additives treatment; (j) The noise spectra for the relevant devices; (k) Detailed energy loss in the D18:L8-BO devices with and without solid additives treatment.

$(n(t) = n(0)/(1 + \left(\frac{t}{\tau_B}\right)^{\gamma})$, where $n(0)$ is the initial density of photogenerated carriers at t=0 and γ is the time-independent parameter), the effective 2nd order recombination coefficient (τ_B) was determined. The initial photogenerated carrier densities (Fig. 2h) are 2.06×10^{16}, 3.30×10^{16}, and 3.59×10^{16}

Table 1 Summary of photovoltaic parameters of the investigated D18:L8-BO binary systems measured under the illumination of AM 1.5 G at 100 mW·cm^{-2}.

Treatment	V_{OC} (V)	J_{SC} (mA·cm^{-2})	$J_{SC\ cal}$ [a] (mA·cm^{-2})	FF (%)	PCE [b] (%)
w/o	0.900	26.48	25.79	76.10	18.14 (17.96±0.08)
2-MN	0.892	26.52	25.83	79.30	18.76 (18.52±0.08)
2,7-MN	0.901	27.28	26.40	81.52	20.19 (20.05±0.10)

[a] $J_{SC\ cal}$ represents the integrated current density obtained from EQE spectra; [b] The average PCE values with standard deviations obtained from 10 independent cells with the active area of 0.048 cm^2.

cm^{-3} for the control, 2-MN- and 2,7-MN-treated devices, respectively, indicating that 2,7-MN facilitates more efficient charge transfer and transport.[37]

Transient photocurrent (TPC) and transient photovoltage (TPV) measurements were further employed to probe charge extraction and recombination dynamics under device operation.[38] TPC measurements (Fig. S11 in ESI) reveal faster photocurrent decay for additive-treated devices, with extraction times decreasing from 0.32 μs (control) to 0.28 μs (2-MN) and 0.23 μs (2,7-MN), indicating more efficient charge extraction. TPV (Fig. S12 in ESI) and charge extraction (CE, Fig. S13 in ESI) measurements provide carrier lifetime τ as a function of carrier density n under open-circuit conditions, $\tau(n)$ (Fig. 2i). Applying the power law dependence of $\tau = \tau_0 (n_0/n)^{\lambda}$, the calculated non-geminate recombination order R values (determined by $R = \lambda+1$) are 1.73, 1.43, and 1.38 for the control, 2-MN- and 2,7-MN-treated D18:L8-BO devices, respectively. This reduced recombination order for the 2,7-MN-treated device indicates suppressed bimolecular recombination and improved charge transport.[39] Moreover, noise spectroscopy (Fig. 2j) reveals a reduced noise exponent of 1.39 for the 2,7-MN-treated device (compared to 1.73 for the control and 1.46 for 2-MN),[40] suggesting diminished trap-assisted recombination, lower defect density, and improved energetic order. To quantitatively analyze energy losses (E_{loss}), the V_{OC} loss was deconvoluted into three components: ΔE_1 (radiative recombination above the bandgap), ΔE_2 (radiative recombination below the bandgap), and ΔE_3 (non-radiative recombination loss) (Figs. S14, S15 and Table S6 in ESI). As shown in Fig. 2(k), the optical band gaps of the control, 2-MN and 2,7-MN-treated devices are 1.185, 1.176, and 1.183 eV, corresponding to ΔE_1 values of 0.258, 0.254, and 0.257 eV, respectively. The ΔE_2 values remain comparable (about 0.08 eV) across all devices, indicating similar charge-transfer state energetics. In contrast, ΔE_3 decreases from 0.205 eV (control) to 0.196 eV (2-MN), and further to 0.191 eV (2,7-MN), demonstrating that the reduced overall energy loss in the 2,7-MN-treated device primarily originates from suppressed non-radiative recombination. Collectively, these results confirm that solid-additive engineering, particularly with 2,7-MN, effectively enhances charge generation, transport, and extraction while minimizing recombination losses, thereby enabling superior device performance. To comprehensive evaluation of this solid-additive approach, we assess the long-term stability (thermal aging at 80 °C dark storage) for the optimal 2-MN and 2,7-MN devices (Fig. S16 in ESI), and noted that both devices show comparable PCE decay.

To verify the volatilization of the solid additives during film formation, Fourier transform infrared spectroscopy was conducted on blend films before and after thermal annealing (80 °C, 5 min). As shown in Fig. S17 (in ESI), the characteristic vibrational peaks of 2-MN and 2,7-MN at around 3110 cm^{-1} disappear after thermal annealing, confirming their complete removal from the blends.[41] Atomic force microscopy (AFM) was employed to investigate the surface morphology of the blend films (Fig. 3a and Fig. S18 in ESI). The root mean square (RMS) roughness decreases from 4.61 nm (control) and 4.39 nm (2-MN) to 2.57 nm for the 2,7-MN-treated film, indicating a smoother surface with finer nanoscale features. This result suggests that 2,7-MN promotes the formation of a more refined fibrillar network. Transmission electron microscopy (TEM) further reveals the internal morphology (Fig. 3b). The additive-free film exhibits pronounced aggregation domains, which are detrimental to exciton dissociation and charge transport. In contrast, both additive-treated films display well-developed fibrous structures, with the 2,7-MN-treated film showing optimal fibril width and domain size. This morphology facilitates the formation of a highly ordered bicontinuous interpenetrating network, enabling efficient exciton utilization, enhanced carrier mobility, and suppressed recombination losses, thereby contributing to improved J_{SC} and FF.[42]

The 2D GIWAXS was performed to investigate the crystallization and molecular packing (Fig. 3c). All blend films exhibit a preferential face-on orientation, evidenced by pronounced (010) π-π stacking peaks in the OOP direction, which is favorable for vertical charge transport. The control film exhibits a broad π-π stacking peak with a shoulder feature, indicative of significant amorphous content. In contrast, the 2-MN-treated and 2,7-MN-treated blend films exhibit stronger diffraction intensity and narrower π-π stacking peaks, suggesting enhanced crystallinity and reduced disorder. Quantitative analysis (Fig. 3d and Table S7 in ESI) shows that the 2,7-MN-treated blend film exhibits a CCL of 44.54 Å and a (010) peak at 1.59 Å^{-1}, corresponding to a π-π stacking distance of 3.94 Å. These results confirm that 2,7-MN promotes tighter molecular packing and improved structural order, which are beneficial for charge transport and recombination suppression.[43] Resonant soft X-ray scattering (RSoXS) measurements were further performed to investigate the phase-separated morphology (Fig. S19 in ESI and Fig. 3e). At an excitation energy of 284.2 eV, corresponding to the 1s-π^* transition of the carbon-carbon double bond (C=C),[44] the control film exhibits pronounced scattering intensity at large length scales. In contrast, both additive-treated films show reduced scattering intensity and predominantly small-length-scale features. Notably, the 2,7-MN-treated film exhibits the smallest phase separation, with characteristic length scales consistent with AFM observations. These results collectively indicate that 2,7-MN enables precise regulation of nanoscale morphology, leading to optimized phase separation and en-

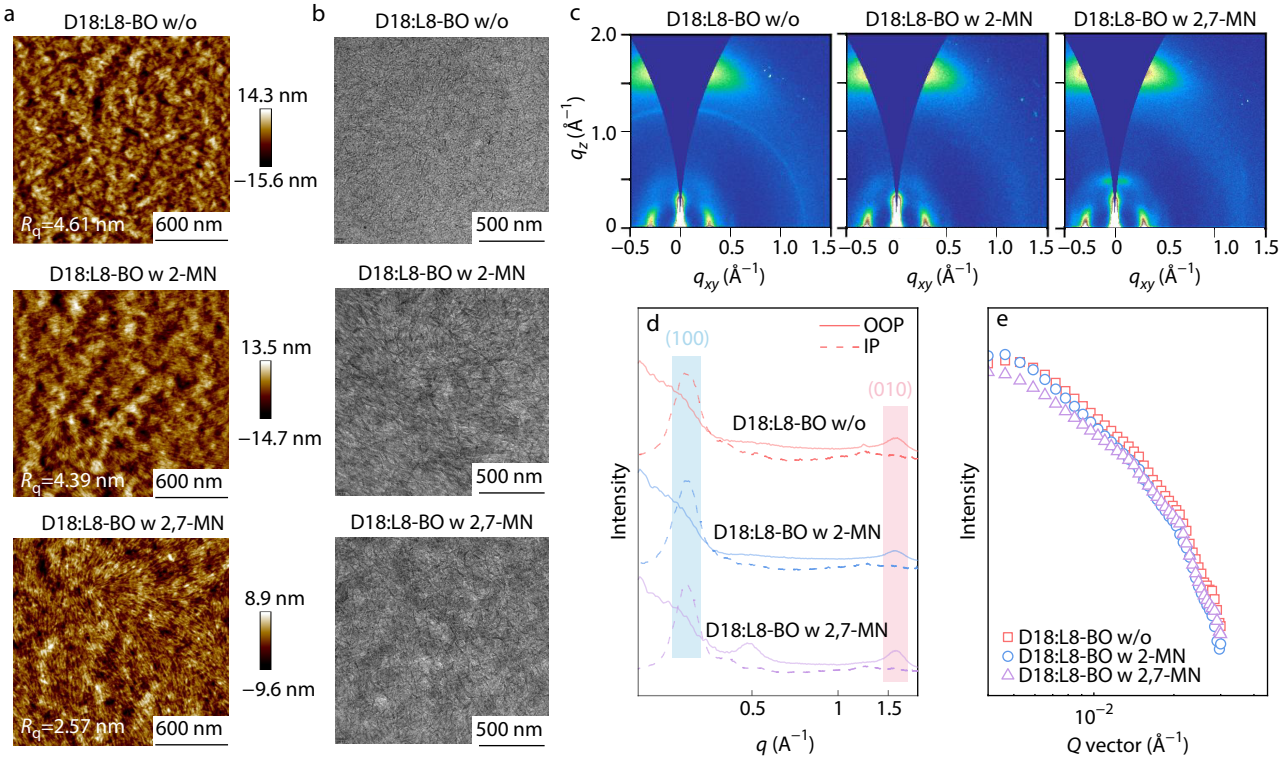


Fig. 3 (a) AFM height images, (b) TEM images, (c) 2D GIWAXS profiles, (d) the corresponding 1D line-cut curves along OOP and IP directions, and (e) the RSoXS profiles of the D18:L8-BO blend films without solid additive, with 2-MN, and 2,7-MN.

hanced device performance.

To elucidate the influence of 2-MN and 2,7-MN on film formation kinetics, resulting in an obvious difference in phase separation as discussed above, *in situ* UV-Vis-NIR spectroscopic measurements were conducted during the film-formation processes of D18:L8-BO with and without additives (Fig. S20 in ESI). The time-resolved spectral evolution is presented as two-dimensional contour plots (Figs. 4a–4c), with corresponding peak-position trajectories shown in Figs. 4(d)–4(f). The evolution of the absorption peak position reveals three distinct stages of film formation: solvent evaporation (stage I), liquid-solid transition (stage II), and film consolidation (stage III).[45] During stage II, a pronounced redshift is observed, indicating progressive molecular stacking and aggregation. Both additives extend the solvent evaporation time (stage I), thereby mitigating premature aggregation that can deteriorate device performance. However, their effects on the subsequent liquid-solid transition (stage II) differ markedly. The 2-MN-treated film exhibits an accelerated transition (0.48 s), whereas 2,7-MN significantly prolongs this stage II from 0.72 s (control) to 1.20 s. The excessively rapid aggregation induced by 2-MN leads to kinetically trapped, disordered domains that are unfavorable for exciton dissociation and charge transport. In contrast, the extended transition enabled by 2,7-MN allows sufficient time for molecular stacking and the formation of a well-defined fibrous interpenetrating network.[46] This controlled aggregation process results in an optimized morphology that supports efficient exciton dissociation and balanced charge transport, ultimately yielding superior photovoltaic performance. Further insight into molecular packing was obtained by deconvoluting the $A_{0\text{-}0}$ and $A_{0\text{-}1}$ vibronic absorption peaks of L8-BO (Fig. S21 in ESI), where $A_{0\text{-}0}$ corresponds to intrachain arrangement and $A_{0\text{-}1}$ to interchain π-π^* transition. The additive-free film exhibits the highest $A_{0\text{-}0}$ / $A_{0\text{-}1}$ ratio (1.89),[34] indicative of dominant intrachain ordering with limited intermolecular coupling. In contrast, films processed with 2-MN and 2,7-MN show reduced ratios of 0.88 and 1.73, respectively, suggesting enhanced intermolecular interactions and suppressed formation of strongly *J*-aggregated states during rapid precipitation. The pronounced *H*-aggregation ($A_{0\text{-}0}/A_{0\text{-}1}$=0.88) and broadened spectral features in the 2-MN-treated film suggest multiple packing motifs, which can be attributed to its relatively weak interaction with L8-BO (binding energy of 0.082 eV). This allows acceptor molecules to pre-assemble into microcrystalline domains during the solvent evaporation stage (stage I), which are then kinetically frozen during the rapid liquid-solid transition. Conversely, the stronger interaction between 2,7-MN and L8-BO (binding energy of 0.197 eV) enables effective molecular intercalation in solution, suppressing excessive self-assembly of the acceptor. The prolonged liquid-solid transition (t_2=1.20 s) further maintains an appropriate stacking order of L8-BO while enhancing D/A intermixing, which is a particularly critical factor for green-solvent-processed systems. Based on these combined insights into molecular packing, film formation kinetics, and final blend morphology, a schematic illustration of the morphological evolution under different additive treatments is presented in Fig. 4(g).

Based upon the above findings that solid additives can effectively retard crystallization and optimize molecular pack-

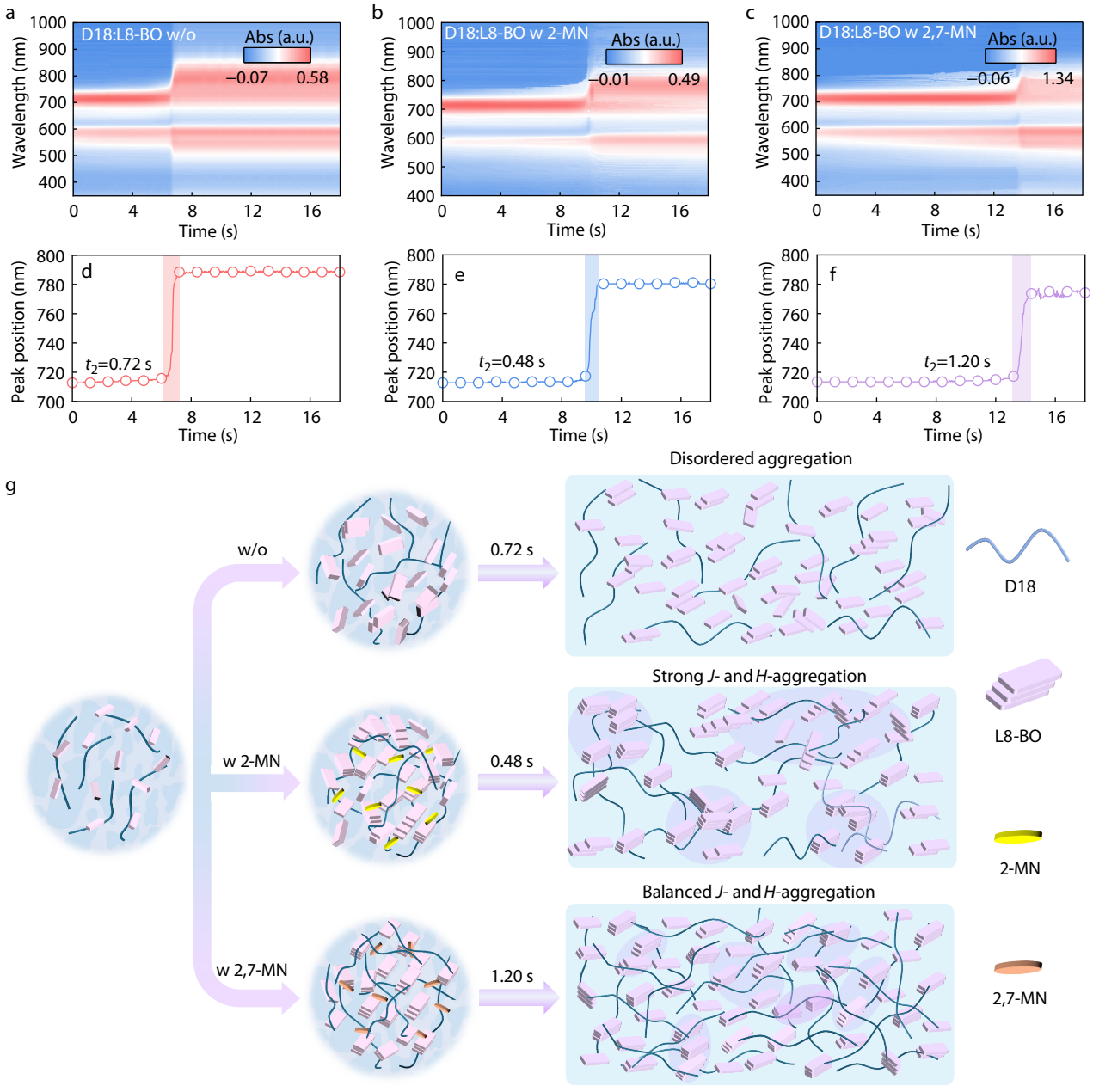


Fig. 4 *In situ* 2D UV-Vis-NIR absorption spectra and temporal evolution of peak positions and intensities of the acceptor in the D18:L8-BO films; (a, d) Without, (b, e) with 2-MN and (c, f) with 2,7-MN films during blade-coating; (g) Schematic illustrating the regulation of the film-formation process and crystallization kinetics for the investigated films.

ing during film formation, we further explored their impact on solution processability under scalable conditions. To achieve precise control over thin-film thickness and morphology, the effects of solution concentration and corresponding blade-coating speed were systematically investigated (Figs. S22–S24 and Tables S8–S10 in ESI).[47,48] Notably, the kinetic regulation of 2,7-MN sustains its effectiveness even under the drastically shortened drying time at the industrially relevant speed of 30 m·min^{-1}. The *in situ* UV-Vis-NIR analysis reveals that the prolonged liquid-solid transition (stage II) provides a critical kinetic buffer, preventing kinetically trapped disorder during rapid solidification, while the strong intermolecular binding between 2,7-MN and L8-BO (0.197 eV) suppresses premature aggregation during the swift solvent evaporation stage (stage I). Furthermore, although the AFM and GIWAXS characterizations were conducted at standard coating speeds, they reveal that 2,7-MN establishes an intrinsically highly ordered and tightly packed network, providing the structural robustness required to withstand the high shear forces inherent to blade-coating. The direct validation of this resilience is evidenced by the maintained PCE of about 19% at 30 m·min^{-1} (Fig. 5a), highlighting the exceptional industrial viability of this solid-additive approach. As shown in Fig. 5(a), a quantitative relationship between coating speed, film thick-

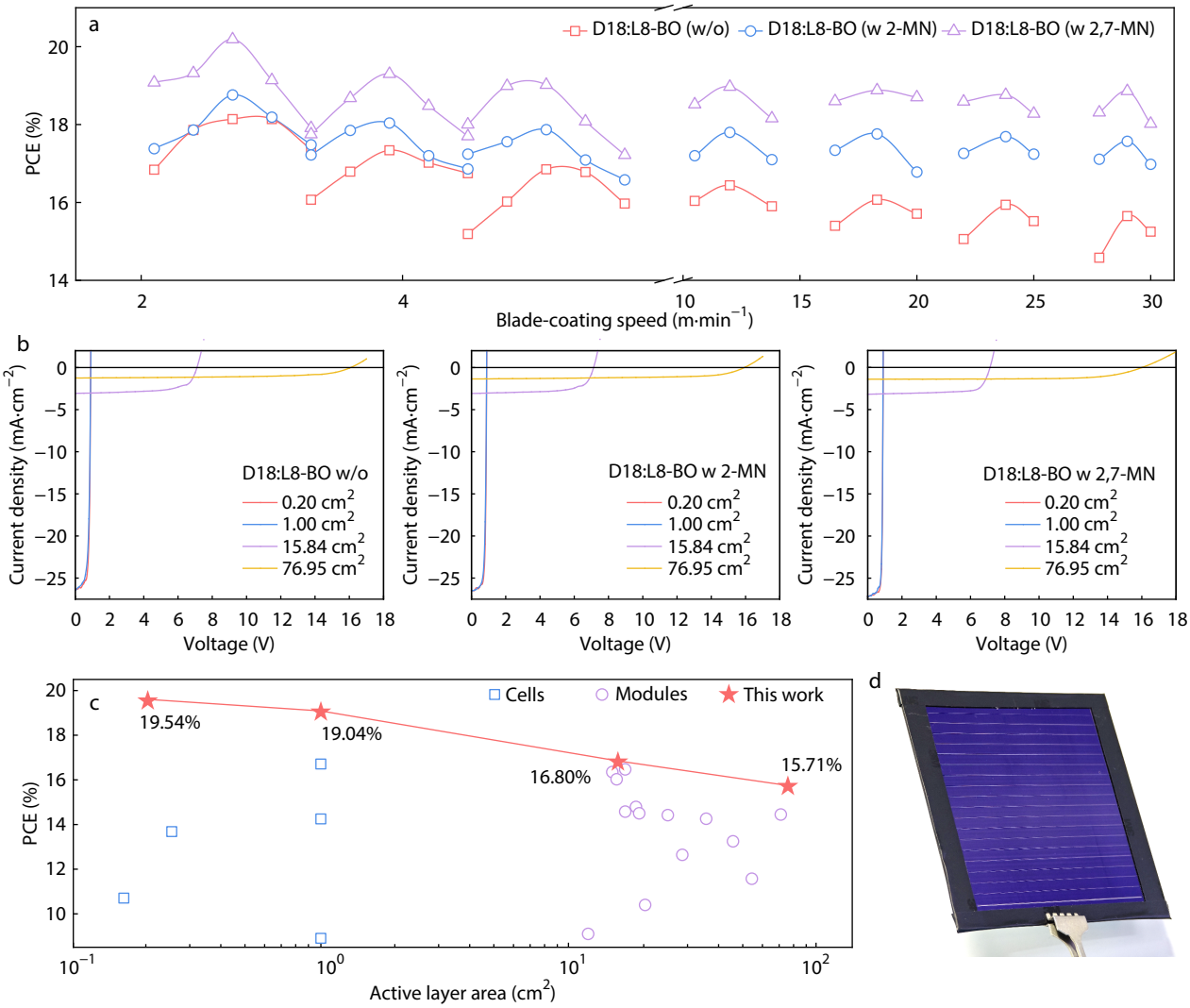


Fig. 5 (a) Extracted PCEs of green-solvent-bladed D18:L8-BO devices with and without solid additives treatment, as a function of blade-coating speed; (b) *J-V* curves of D18:L8-BO devices and modules with and without solid additives treatment, with active areas of 0.20, 1.00, 15.84, and 76.95 cm^2; (c) Efficiency comparison of our results (red stars) and reported results in the literature (blue and purple circles) of green-solvent-bladed OSCs; (d) A picture of a large-area (76.95 cm^2) green-solvent-bladed module with eighteen sub-cells.

ness, and device performance was established. For control devices, the PCE decreases markedly from 18.14% to 15.65% with increasing coating speed, despite comparable film thicknesses, indicating insufficient morphological robustness. In contrast, devices processed with solid additives exhibit significantly improved tolerance to high-speed coating. Notably, 2,7-MN-treated devices retain a high PCE of 18.86% even at a coating speed of 30.0 m·min^{-1}, demonstrating that 2,7-MN effectively mitigates performance losses under high-speed coating conditions.

To further assess scalability,[49] large-area devices (0.20 and 1.00 cm^2) and modules (15.84 and 76.95 cm^2) based on the D18:L8-BO system were fabricated without and with solid-additive treatment. The optimal *J-V* curves are illustrated in Fig. 5(b), with the photovoltaic parameters listed in Table S11 (in ESI). Across the four different active areas, the 2,7-MN-treated systems consistently deliver excellent PCEs. In particular, the 2,7-MN-treated D18:L8-BO module with an active area of 76.95 cm^2 achieves a PCE of 15.71%, significantly outperforming the 2-MN-treated (13.73%) and additive-free (12.22%) counterparts. Compared with previously reported green-solvent-processed, blade-coated solar cells and modules, the devices presented here exhibit highly competitive efficiencies (Fig. 5c and Tables S12, S13 in ESI). A photograph of the large-area module (76.95 cm^2) consisting of 18 sub-cells is shown in Fig. 5(d), where the active layer exhibits excellent thickness uniformity. These results highlight that the combination of environmentally friendly solvents and rationally designed solid additives, particularly 2,7-MN, provides an effective strategy for morphology control, enabling high-efficiency, process-robust solar modules suitable for industrial-scale manufacturing.

CONCLUSIONS

In summary, we have developed an effective solid-additive engineering strategy to enable high-efficiency, green-solvent-pro-

cessed OSCs with excellent process robustness and scalability. By introducing two environmentally benign solid additives, 2-MN and 2,7-MN, into the D18:L8-BO system, we systematically elucidate how additive molecular structure governs intermolecular interactions, crystallization kinetics, and morphology evolution during film formation. Both experimental and theoretical results reveal that the symmetric structure and stronger binding affinity of 2,7-MN enable it to act as an efficient kinetic regulator, prolonging the liquid-solid transition, suppressing premature aggregation, and guiding the formation of a highly ordered bicontinuous interpenetrating network. This optimized morphology simultaneously enhances exciton dissociation, promotes balanced charge transport, and suppresses both geminate and non-geminate recombination, leading to a promising PCE of 20.19% under blade-coating conditions. Importantly, the morphology control enabled by 2,7-MN remains effective under high-speed coating (up to 30 m·min^{-1}), maintaining PCEs approaching 19%, which highlights its compatibility with industrially relevant processing. Furthermore, large-area modules with active areas up to 76.95 cm^2 deliver PCEs of 15.71%, demonstrating excellent scalability and film uniformity. Beyond performance metrics, this work provides fundamental insights into the interplay between additive structure, intermolecular interactions, and non-equilibrium film-formation dynamics in green-solvent systems. Overall, this study offers a general and scalable strategy for achieving high-efficiency OSCs while adhering to environmental and manufacturing constraints, paving the way toward sustainable and industrially viable organic photovoltaic technologies.

Conflict of Interests

The authors declare no interest conflict.

Electronic Supplementary Information

Electronic supplementary information (ESI) is available free of charge in the online version of this article at http://doi.org/10.1007/s10118-026-3838-8.

Data Availability Statement

The data that support the findings of this study are available from the corresponding author upon reasonable request.

ACKNOWLEDGMENTS

This work was financially supported by the National Natural Science Foundation of China (NSFC) (Nos. 22279094 and 22409149), Anhui Province Key Laboratory for Control and Application of Optoelectronic Information Materials (No. OIM-2024-01), and Key Laboratory for Preparation and Application of Ordered Structural Materials of Guangdong Province. The authors extend their gratitude to the technical staff from Scientific Compass www.shiyanjia.com for providing invaluable assistance with the FTIR analysis. We thank the Core Facility of Wuhan University for the AFM and TEM measurements. The authors thank the resonant soft X-ray scattering beamline (Jinhua) BL05U-B of Hefei Light Source, jointly constructed by the Zhejiang Institute of Optoelectronics and the National Synchrotron Radiation Laboratory of the University of Science and Technology of China.

REFERENCES

1 Xie, D.; Wu, B.; Wu, Q.; Deng, B.; Li, J.; Chen, Z.; Zhu, J.; Xia, R.; Pan, L.; Liu, K.; Jiang, Q.; Feng, H.; Yuan, X.; Zhang, Y.; Jiang, Q.; Liu, D.; Xu, T.; Li, H.; Huang, F.; Cao, Y.; Duan, C. Scalable polymer for large-area semitransparent organic photovoltaics. *Joule* **2025**, *9*, 102173.
2 Lu, X.; Xie, C.; Liu, Y.; Zheng, H.; Feng, K.; Xiong, Z.; Wei, W.; Zhou, Y. Increase in the efficiency and stability of large-area flexible organic photovoltaic modules *via* improved electrical contact. *Nat. Energy* **2024**, *9*, 793–802.
3 Jinno, H.; Fukuda, K.; Xu, X.; Park, S.; Suzuki, Y.; Koizumi, M.; Yokota, T.; Osaka, I.; Takimiya, K.; Someya, T. Stretchable and waterproof elastomer-coated organic photovoltaics for washable electronic textile applications. *Nat. Energy* **2017**, *2*, 780–785.
4 Corzo, D.; Rosas-Villalva, D.; C, A.; Tostado-Blázquez, G.; Alexandre, E. B.; Hernandez, L. H.; Han, J.; Xu, H.; Babics, M.; De Wolf, S.; Baran, D. High-performing organic electronics using terpene green solvents from renewable feedstocks. *Nat. Energy* **2023**, *8*, 62–73.
5 Shi, H. Y.; Xing, L.; Chen, M. X.; Chen, Z. Y.; Deng, M. W.; Xu, L. Y.; Wu, X. H.; Yang, X. R.; Shao, Y. M.; Papkovskaya, E. D.; Luponosov, Y.; Sun, R.; Min, J. Pendant Y-series acceptors with well-controlled morphology enabled high performance and stability all-polymer solar cells. *Chinese J. Polym. Sci.* **2025**, *43*, 1516–1526.
6 Burgués-Ceballos, I.; Lucera, L.; Tiwana, P.; Ocytko, K.; Tan, L. W.; Kowalski, S.; Snow, J.; Pron, A.; Bürckstümmer, H.; Blouin, N.; Morse, G. Transparent organic photovoltaics: a strategic niche to advance commercialization. *Joule* **2021**, *5*, 2261–2272.
7 Chen, H.; Huang, Y.; Zhang, R.; Mou, H.; Ding, J.; Zhou, J.; Wang, Z.; Li, H.; Chen, W.; Zhu, J.; Cheng, Q.; Gu, H.; Wu, X.; Zhang, T.; Wang, Y.; Zhu, H.; Xie, Z.; Gao, F.; Li, Y.; Li, Y. Organic solar cells with 20.82% efficiency and high tolerance of active layer thickness through crystallization sequence manipulation. *Nat. Mater.* **2025**, *24*, 444–453.
8 Wang, Y.; Wen, J.; Zhong, Y.; Fu, L.; You, Z.; Li, H.; Han, G.; Han, W.; Liu, J.; Zhang, H.; Feng, Y.; Li, H.; Liu, W.; Zhang, J.; Han, K.; Liu, Y. Homology-guided zwitterionic interlayers for 21% efficiency non-fullerene organic solar cells. *Adv. Mater.* **2026**, *38*, e20669.
9 Fu, J.; Li, H.; Liu, H.; Huang, P.; Chen, H.; Fong, P. W. K.; Dela Peña, T. A.; Li, M.; Lu, X.; Cheng, P.; Xiao, Z.; Lu, S.; Li, G. Two-step crystallization modulated through acenaphthene enabling 21% binary organic solar cells and 83.2% fill factor. *Nat. Energy* **2025**, *10*, 1251–1261.
10 Basu, R.; Gumpert, F.; Lohbreier, J.; Morin, P. O.; Vohra, V.; Liu, Y.; Zhou, Y.; Brabec, C. J.; Egelhaaf, H. J.; Distler, A. Large-area organic photovoltaic modules with 14.5% certified world record efficiency. *Joule* **2024**, *8*, 970–978.
11 Carlé, J. E.; Helgesen, M.; Hagemann, O.; Hösel, M.; Heckler, I. M.; Bundgaard, E.; Gevorgyan, S. A.; Søndergaard, R. R.; Jørgensen, M.; García-Valverde, R.; Chaouki-Almagro, S.; Villarejo, J. A.; Krebs, F. C. Overcoming the scaling lag for polymer solar cells. *Joule* **2017**, *1*, 274–289.
12 Zhang, B.; Yang, F.; Li, Y. Recent progress in large-area organic solar cells. *Small Sci.* **2023**, *3*, 2300004.
13 Han, J.; Xu, H.; Corzo, D.; Sharma, A.; Baran, D. Pathways to commercially viable organic photovoltaic materials. *Nat. Mater.* **2026**, *25*, 725–736.
14 Zhou, M.; Xu, X.; Wang, D.; Song, J.; Qiao, J.; Zhang, R.; Wu, Y.;

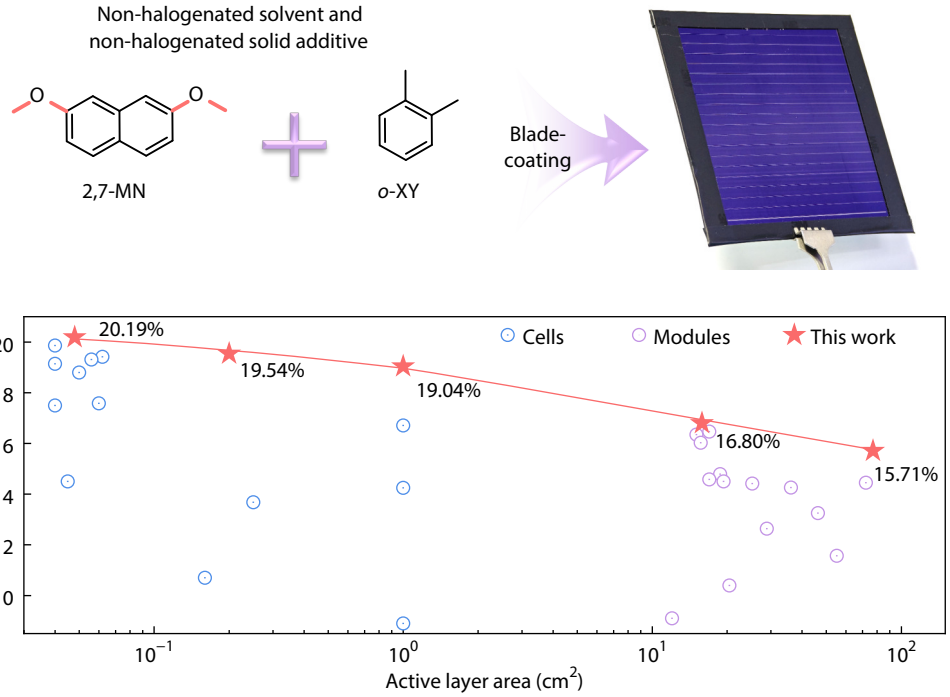
Graphical Abstract

Solid-additive-regulated Non-equilibrium Film Formation Enables Highly-efficient Green-solvent-printed Binary Organic Solar Cells and Solar Modules

Shan-Hua Zhang, Rui Sun, Zi-Cheng Xing, Jia-Wang Qiu, Lin-Yong Xu, Yu-Hao Liu, Tian-Rui Qu, Xin-Rong Yang, and Jie Min

Wuhan University; Shantou University; Anhui Normal University

A non-halogenate solid-additive strategy is developed to regulate non-halogenated solvent-processed active layer formation and balance molecular aggregation in organic photovoltaics during blade-coating, delivering record efficiencies of 20.19% on small-area (0.048 cm^2) devices and 15.71% on large-area (76.95 cm^2) modules.



Chinese J. Polym. Sci. 2026 *https://doi.org/10.1007/s10118-026-3838-8*

Wang, T.; Cui, J.; Hall, C. R.; Yin, H.; Du, X.; Qin, W.; Gao, K.; Chen, F.; Wei, Z.; Ashokkumar, M.; Smith, T. A.; Zhang, K.; Sun, Y.; Hao, X. Sonication-induced J-aggregation in nonhalogenated solvents boosts exciton delocalization for high-efficiency organic solar cells. *Nat. Commun.* **2025**, *16*, 10458.

15 Harillo-Baños, A.; Fan, Q.; Riera-Galindo, S.; Wang, E.; Inganäs, O.; Campoy-Quiles, M. High-throughput screening of blade-coated polymer: polymer solar cells: solvent determines achievable performance. *ChemSusChem* **2022**, *15*, e202101888.

16 Yang, S.; Chen, X.; Pan, Y.; Fang, J.; Han, Y.; Wang, Z.; Qian, F.; Qi, W.; Shui, K.; Zhang, Q.; Guo, F.; Sun, Y.; Ma, C. Q.; Luo, Q. High cell to module efficiency remaining ratio of ≈90% for the 100 cm^2 fully roll-to-roll gravure printed flexible organic solar cells from non-halogenated solvent. *Adv. Mater.* **2025**, *37*, 2500115.

17 Chen, H.; Zhang, R.; Chen, X.; Zeng, G.; Kobera, L.; Abbrent, S.; Zhang, B.; Chen, W.; Xu, G.; Oh, J.; Kang, S. H.; Chen, S.; Yang, C.; Brus, J.; Hou, J.; Gao, F.; Li, Y.; Li, Y. A guest-assisted molecular-organization approach for >17% efficiency organic solar cells using environmentally friendly solvents. *Nat. Energy* **2021**, *6*, 1045–1053.

18 He, H.; Li, X.; Zhang, J.; Chen, Z.; Gong, Y.; Zhuo, H.; Wu, X.; Li, Y.; Wang, S.; Bi, Z.; Song, B.; Zhou, K.; Liang, T.; Ma, W.; Lu, G.; Ye, L.; Meng, L.; Zhang, B.; Li, Y.; Li, Y. Dynamic hydrogen-bonding enables high-performance and mechanically robust organic solar cells processed with non-halogenated solvent. *Nat. Commun.* **2025**, *16*, 787.

19 Song, J.; Zhang, C.; Li, C.; Qiao, J.; Yu, J.; Gao, J.; Wang, X.; Hao, X.; Tang, Z.; Lu, G.; Yang, R.; Yan, H.; Sun, Y. Non-halogenated solvent-processed organic solar cells with approaching 20 % efficiency and improved photostability. *Angew. Chem. Int. Ed.* **2024**, *63*, e202404297.

20 Wang, H.; Liu, S.; Li, H.; Li, M.; Wu, X.; Zhang, S.; Ye, L.; Hu, X.; Chen, Y. Green printing for scalable organic photovoltaic modules by controlling the gradient Marangoni flow. *Adv. Mater.* **2024**, *36*, 2313098.

21 Machui, F.; Lucera, L.; Spyropoulos, G. D.; Cordero, J.; Ali, A. S.; Kubis, P.; Ameri, T.; Voigt, M. M.; Brabec, C. J. Large area slot-die coated organic solar cells on flexible substrates with non-

halogenated solution formulations. *Sol. Energy Mater. Sol. Cells* **2014**, *128*, 441−446.
22 Zhao, H.; Naveed, H. B.; Lin, B.; Zhou, X.; Yuan, J.; Zhou, K.; Wu, H.; Guo, R.; Scheel, M. A.; Chumakov, A.; Roth, S. V.; Tang, Z.; Müller-Buschbaum, P.; Ma, W. Hot hydrocarbon-solvent slot-die coating enables high-efficiency organic solar cells with temperature-dependent aggregation behavior. *Adv. Mater.* **2020**, *32*, 2002302.
23 Zhang, L.; Zhang, J.; Ma, Y.; Guo, X.; Huang, H.; Bi, Z.; Wang, Y.; Zhang, Y.; Xie, C.; Luo, W.; Hu, X.; Ma, W.; Yuan, Y. Improving efficiency and flexibility of non-halogenated solvent-processed dual-layer organic solar cells through solvent vapor annealing. *Org. Electron.* **2024**, *130*, 107075.
24 Song, J.; Li, Y.; Cai, Y.; Zhang, R.; Wang, S.; Xin, J.; Han, L.; Wei, D.; Ma, W.; Gao, F.; Sun, Y. Solid additive engineering enables high-efficiency and eco-friendly all-polymer solar cells. *Matter* **2022**, *5*, 4047−4059.
25 Liang, Q.; Li, H.; Xu, W.; Lu, J.; Ma, R.; Bai, Q.; Sun, X.; Chen, M.; Zhu, L.; Liu, Q.; Guo, Y.; Zhang, G.; Xue, Q.; Iwan, A.; Cheng, P.; Hu, H.; Wang, H.; Chen, J.; Niu, L.; Sun, H. Dual-asymmetric solid additive enables eco-friendly all-polymer solar cells with over 19% efficiency and excellent stability. *Angew. Chem. Int. Ed.* **2025**, *64*, e202425267.
26 Dahiya, H.; Kumar, D.; Sharma, G. D.; Karak, S. The emerging role of solid additives in advancing stability and performance of organic solar cells. *Energy Technol.* **2026**, *14*, e202502517.
27 Xu, X.; Yu, L.; Yan, H.; Li, R.; Peng, Q. Highly efficient non-fullerene organic solar cells enabled by a delayed processing method using a non-halogenated solvent. *Energy Environ. Sci.* **2020**, *13*, 4381−4388.
28 Wu, S.; Xu, H.; Wang, H.; Liu, X.; Tu, L.; Zhang, W.; Chen, Y.; Song, X.; Shi, Y. Isomerized dithienopyrazine-based solid additive enables organic solar cells with 20.5% efficiency. *Angew. Chem. Int. Ed.* **2026**, *65*, e6458866.
29 Yao, H.; Qian, D.; Zhang, H.; Qin, Y.; Xu, B.; Cui, Y.; Yu, R.; Gao, F.; Hou, J. Critical role of molecular electrostatic potential on charge generation in organic solar cells. *Chin. J. Chem.* **2018**, *36*, 491−494.
30 Wang, X.; Wu, J.; Zhao, S.; Chen, M.; Shi, T.; Xie, X.; Bai, Q.; Xie, J.; Zhang, L.; Ma, D.; Chen, J. Elevating dielectric constant *via* additive engineering: achieving 19.23% certified efficiency in thick-film binary organic solar cells. *Joule* **2025**, *9*, 102135.
31 Li, C.; Zhou, J.; Song, J.; Xu, J.; Zhang, H.; Zhang, X.; Guo, J.; Zhu, L.; Wei, D.; Han, G.; Min, J.; Zhang, Y.; Xie, Z.; Yi, Y.; Yan, H.; Gao, F.; Liu, F.; Sun, Y. Non-fullerene acceptors with branched side chains and improved molecular packing to exceed 18% efficiency in organic solar cells. *Nat. Energy* **2021**, *6*, 605−613.
32 Xu, L. Y.; Gao, Y.; Sun, R.; Xing, Z.; Xiao, B.; Yang, X.; Shao, Y.; Chang, B.; Wu, X.; Xiao, B.; Zhang, M.; Min, J. Controlled-disorder asymmetrical donors enable efficient all-small-molecule solar cells with excellent solution-processability. *Angew. Chem. Int. Ed.* **2026**, *65*, e19713.
33 Zheng, B.; Yue, Y.; Ni, J.; Zhou, X.; He, Y.; Gui, X.; Shen, H.; Jing, Y.; Zhao, J.; Zhang, J.; Zhang, Y.; Wang, J.; Jiang, L.; Huo, L. An efficient one-arrow-two-hawks strategy achieves high efficiency and stable batch variance for benzodifuran-based polymer solar cells. *Adv. Funct. Mater.* **2023**, *33*, 2300981.
34 Song, H.; Yue, Y.; Gui, X.; Sun, S.; Yang, Z.; Zheng, B.; Shen, H.; Wang, J.; Zhang, J.; Huo, L. Strategic engineering of H-/J-aggregation equilibrium in non-fullerene acceptors toward high-performance organic photovoltaics. *Energy Environ. Sci.* **2026**, *19*, 1703−1714.
35 Sun, R.; Wu, Y.; Yang, X.; Gao, Y.; Chen, Z.; Li, K.; Qiao, J.; Wang, T.; Guo, J.; Liu, C.; Hao, X.; Zhu, H.; Min, J. Single-junction organic solar cells with 19.17% efficiency enabled by introducing one asymmetric guest acceptor. *Adv. Mater.* **2022**, *34*, 2110147.
36 Jiang, Y.; Sun, S.; Xu, R.; Liu, F.; Miao, X.; Ran, G.; Liu, K.; Yi, Y.; Zhang, W.; Zhu, X. Non-fullerene acceptor with asymmetric structure and phenyl-substituted alkyl side chain for 20.2% efficiency organic solar cells. *Nat. Energy* **2024**, *9*, 975−986.
37 Sun, R.; Wu, Q.; Guo, J.; Wang, T.; Wu, Y.; Qiu, B.; Luo, Z.; Yang, W.; Hu, Z.; Guo, J.; Shi, M.; Yang, C.; Huang, F.; Li, Y.; Min, J. A layer-by-layer architecture for printable organic solar cells overcoming the scaling lag of module efficiency. *Joule* **2020**, *4*, 407−419.
38 Shao, Y.; Sun, R.; Wang, W.; Yang, X.; Sun, C.; Li, Y.; Min, J. Low-cost organic photovoltaic materials with great application potentials enabled by developing isomerized non-fused ring acceptors. *Sci. China Chem.* **2023**, *66*, 1101−1110.
39 Gasparini, N.; Jiao, X.; Heumueller, T.; Baran, D.; Matt, G. J.; Fladischer, S.; Spiecker, E.; Ade, H.; Brabec, C. J.; Ameri, T. Designing ternary blend bulk heterojunction solar cells with reduced carrier recombination and a fill factor of 77%. *Nat. Energy* **2016**, *1*, 16118.
40 Kumar, A.; Bansode, U.; Ogale, S.; Rahman, A. Understanding the thermal degradation mechanism of perovskite solar cells *via* dielectric and noise measurements. *Nanotechnology* **2020**, *31*, 365403.
41 Hu, T.; Chen, L.; Miao, W.; Li, C.; Song, J.; Liao, Y.; Liang, J.; Xiong, J.; Wang, X.; Sun, Y.; Yan, H.; Yang, R. Benzothieno [1,2-*b*] furan: an atomically symmetric-breaking volatile solid additive for high-performance thick-film planar heterojunction organic solar cells. *Sci. China Chem.* **2026**, *69*, 1273−1281.
42 Sun, R.; Wang, T.; Fan, Q.; Wu, M.; Yang, X.; Wu, X.; Yu, Y.; Xia, X.; Cui, F.; Wan, J.; Lu, X.; Hao, X.; Jen, A. K.; Spiecker, E.; Min, J. 18.2%-efficient ternary all-polymer organic solar cells with improved stability enabled by a chlorinated guest polymer acceptor. *Joule* **2023**, *7*, 221−237.
43 Yao, S.; Yang, L.; Shi, S.; Zhou, Y.; Long, M.; Zhang, W.; Cai, S.; Huang, C.; Liu, T.; Zou, B. A two-in-one annealing enables dopant free block copolymer based organic solar cells with over 16% efficiency. *Chin. J. Chem.* **2023**, *41*, 672−678.
44 Xu, S.; He, Q.; Xue, X.; Deng, J.; Han, F.; Xie, F.; Jiao, X.; Zhou, L.; Zeng, R.; Wang, Z.; Zhang, M.; Zhu, L.; Jing, H.; Zhang, Y.; Liu, F. Construction of shamrock-shaped giant molecule acceptors for efficient organic solar cells. *Angew. Chem. Int. Ed.* **2025**, *64*, e202507616.
45 Chen, Z.; Zhang, S.; Sun, R.; Mei, L.; Yang, W.; Xing, Z.; Yang, X.; Xiao, B.; Wu, X.; Chen, X.; Min, J. Enhanced ε_r/L_D and improved acceptor crystal growth enable all-polymer solar cells with outstanding efficiency, stability, and processability from a chlorinated-dimer diluent additive. *Energy Environ. Sci.* **2026**, *19*, 946−957.
46 Wei, L.; Zhan, L.; Yang, Y.; Chen, T.; Yu, J.; Sun, X.; Hu, H.; Sun, R.; Min, J.; Li, Y.; Wu, J.; Che, J.; Zhang, G.; Zhang, J.; Li, Y.; Yin, S.; Chen, H. Precise morphology control *via* backbone-derived solid additive enables binary organic solar cells to achieve 20% efficiency and thick-film compatibility. *Adv. Mater.* **2026**, *38*, e18516.
47 Sun, R.; Wang, T.; Yang, X.; Wu, Y.; Wang, Y.; Wu, Q.; Zhang, M.; Brabec, C. J.; Li, Y.; Min, J. High-speed sequential deposition of photoactive layers for organic solar cell manufacturing. *Nat. Energy* **2022**, *7*, 1087−1099.
48 Shao, Y.; Gao, Y.; Sun, R.; Yang, X.; Zhang, M.; Liu, S.; Min, J. A high-performance organic photovoltaic system with versatile solution processability. *Adv. Mater.* **2024**, *36*, 2406329.
49 Dong, S.; Jia, T.; Zhang, K.; Jing, J.; Huang, F. Single-component non-halogen solvent-processed high-performance organic solar cell module with efficiency over 14%. *Joule* **2020**, *4*, 2004−2016.

https://doi.org/10.1007/s10118-026-3838-8